# ThunderKAT S-band observations

Evangelia (Lilia) Tremou on behalf of the ThunderKAT team
etremou@nrao.edu

March 7, 2023

**Abstract**

We present the results from the our recent MeerKAT S–band observations taken as part of the ThunderKAT monitoring program[1] (Fender et al., 2016). The main target of these observations is a transient X-ray binary discovered recently with Monitor of All-sky X-ray Image (MAXI; Matsuoka et al., 1990). As part of ThunderKAT, the X-ray binary is monitored weekly in L-band (1.28GHz) and its evolution is reported by Bahramian et al. 2023, submitted to ApJL.

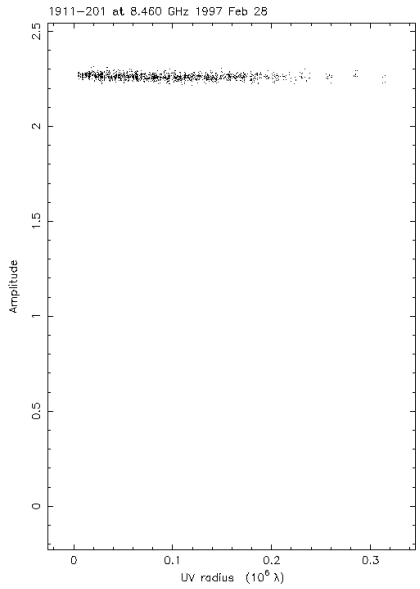


Figure 1: Amplitude-UV distance plot of the secondary calibrator as it has been reported at the VLA X-band. Important to help us confirm that the secondary calibrator won't be resolved at S-band. Adapted from http://www.vla.nrao.edu/astro/calib/manual-obsolete/calplots/3.7cmB/1911-201.uv.png

## 1 Observations

MeerKAT S-band observations took place on November 20, 2022 using 60 antennas in total for 15 minutes on source, centered on the field of of the newly discovered X-ray binary. The receiver was tuned at S-3 sub-band, 2843.8 MHz. J1939-6342 was observed as primary calibrator for bandpass and flux scale corrections and two scans of J1911-2006 were used as secondary calibrator, Figures 1 and 2 probe the point source like structure of the phase calibrator. A summary of the observation is shown in Figure 3. The data were transferred from the SARAO archive to the ilifu/IDIA cluster for processing applying the *cam* and *data_lost* flagsets and averaging them to 4096 channels.

[1] http://www.thunderkat.uct.ac.za/

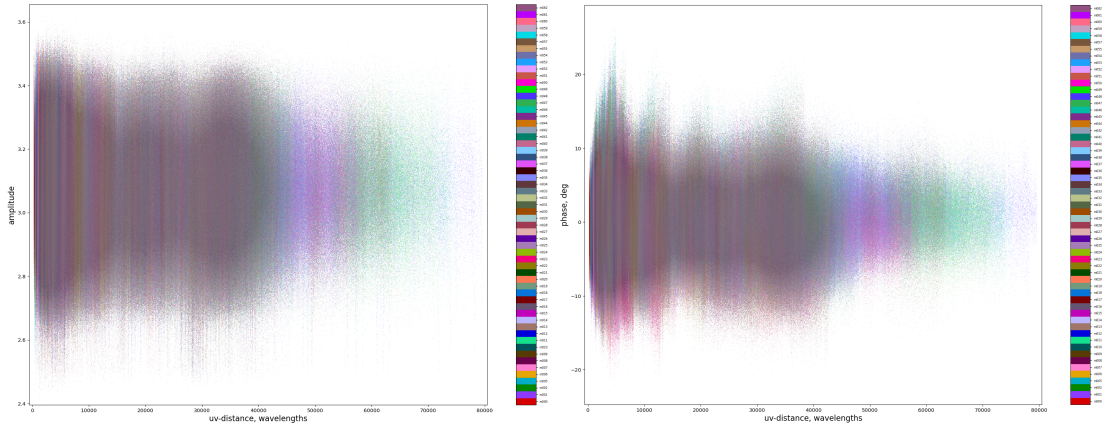


Figure 2: Amplitude-UV distance plot (**left**) of the secondary calibrator, J1911-2006, and the phase as a function of UV distance (**right**) per antenna using the XX correlation data [a] of the current S3 sub-band data set.

[a]The plots were produced using https://github.com/ratt-ru/shadeMS

# 2 Data Processing

## 2.1 Raw data inspection and Flagging

The raw data were retrieved in Measurement Set (MS) format and were inspected in detail using the *rfigui*[2] and the *aoqplot*[3] software routines for quick visualization. Radio frequency interference (RFI) was noticed in 2483.5-2500.0 MHz as a continuous signal which seems to dominate the short baselines and it possibly originates by the GlobalStar down-link [4]. An example can be seen for the target field of our observations in Figure 4. The frequency scatter is shown in the Figure 5, noting the low visibility count on the cross-hands (blue and green) and the interference at $\sim$ 2.5GHz. We used the *AOFlagger*[5] software (Offringa et al., 2012) to remove this RFI feature which is the main RFI source in these observations.

```
Observer:                  Evangelia Tremou
Telescope:                 MeerKAT
Project:                   20221119-0015
Beginning of Observation:  2022-11-20 11:42:51.416 (ISO) -- 59903.48809508933 (MJD)
Observation length:        1547.0s (0.43 h)
Mean integration time:     7.98 s
Number of correlation
polarization products:     [4]

ROW   ID    NAME          RA            DEC
0     0
1     1
2     2

ROW   CHANS         WIDTH[MHz]          REF_FREQ[MHz]
0     4096          0.213623046875      2843.843460083008
```

Figure 3: Summary of S3 -band observations taken at the field of a regularly monitored X-ray binary on November 2022 as part of the ThunderKAT large survey program.

Figure 6 presents the statistics of RFI per antenna and per baseline. In average only 7% of the data are contaminated due to the RFI with the antenna m036 being exceptional reaching $\sim$ 17%. In the right panel of the Figure 6, the short baselines seem to be affected more ($\sim$31%) than the long ones ($\sim$4%).

[2]https://sourceforge.net/p/aoflagger/wiki/rfigui/
[3]https://sourceforge.net/p/aoflagger/wiki/aoqplot/
[4]https://science.nrao.edu/facilities/vla/observing/RFI/S-Band
[5]https://sourceforge.net/p/aoflagger/wiki/Home/

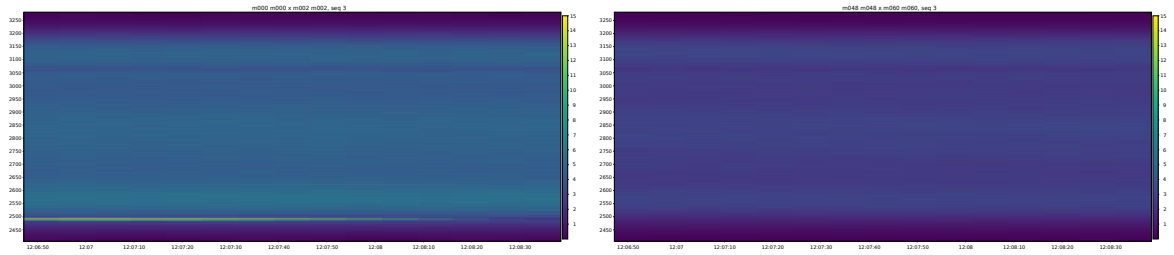

Figure 4: Waterfall plots showing the Radio Frequency Interference (RFI) seen at $\sim$ 2.5 GHz due to GlobalStar downlink in short **(left)** and long baselines **(right)** for the target field.

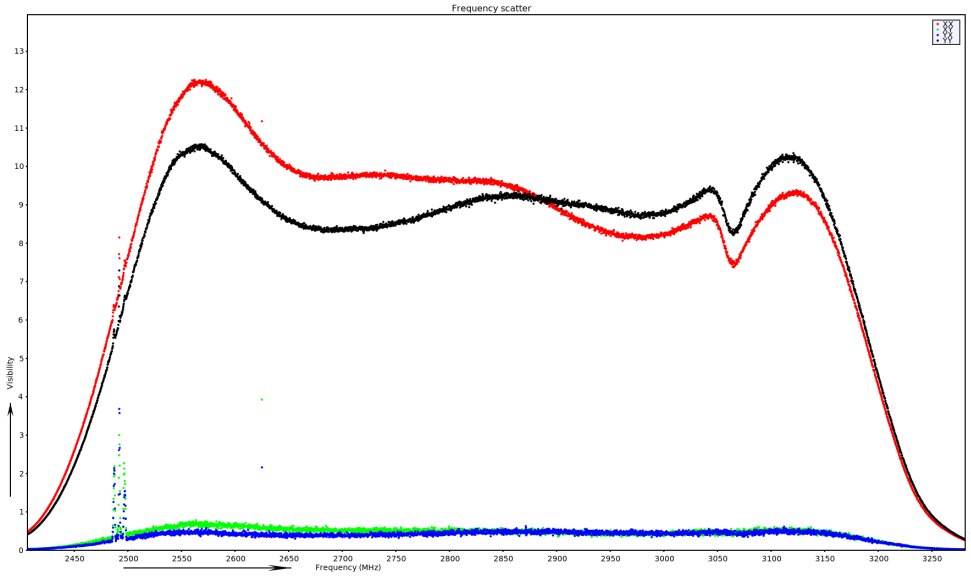


Figure 5: Frequency scatter in raw data colorized by polarization output. Noting the low visibility count on the cross-hans (blue and green).

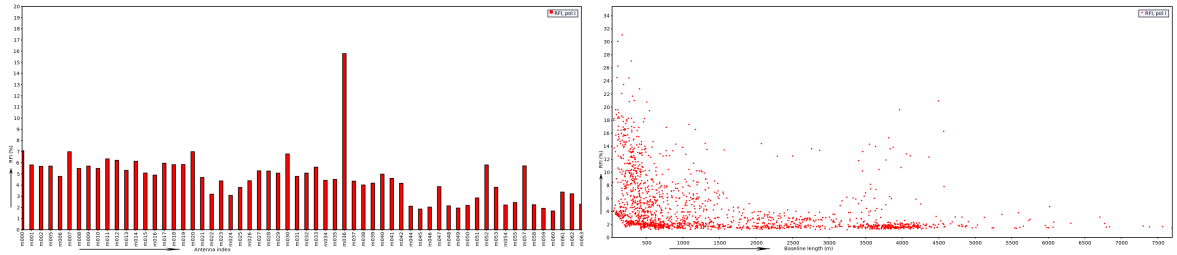

Figure 6: Radio Frequency Interfernce (RFI) occupancy statistics per antenna (**left**) and per baseline (**right**).

## 2.2 Calibration

The *CASA* v5.6.2 (McMullin et al., 2007) package was used to perform the standard calibration steps such as antenna based delays, bandpass and complex gain corrections from the primary and the secondary calibrator, respectively. The antenna–based delays are plotted[6] in Figure 7 ranging within $\pm$ 0.15 nano seconds. Figure 8 shows the amplitude gains (left) and the phase solutions (right) that have been derived using the single scan of the primary calibrator. Each antenna is plotted with different color showing the stability of the bandpass over the observing course. Antenna m047 shows some phase pattern $\sim \pm$ 5deg but overall the phases show a smooth profile.

The reference gains corrections were applied to the target field following a final data examination for remaining RFI in the target field using the CASA auto flaggers (rflag and tfcrop).

[6] ragavi-gains used for visualizing the calibration solutions (`https://ragavi.readthedocs.io/`)

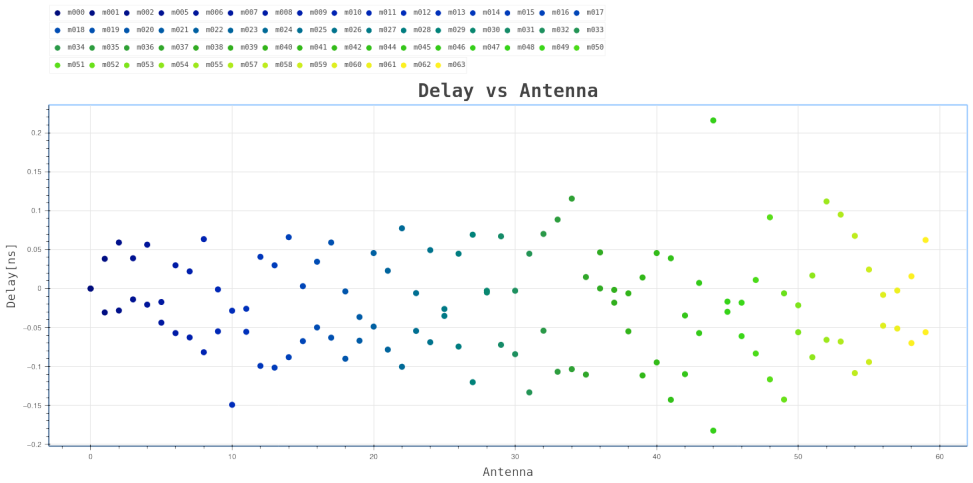


Figure 7: Antenna delays using the bandpass (primary calibrator).

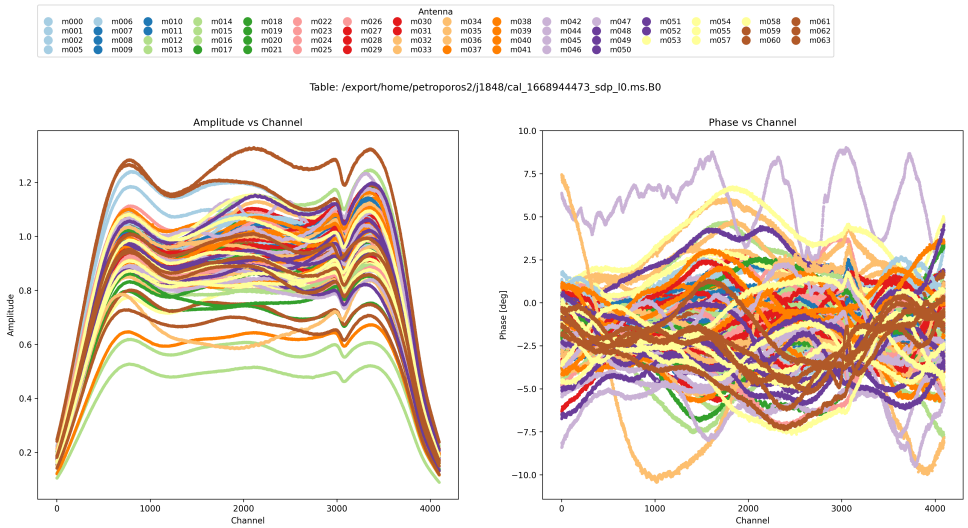


Figure 8: Amplitude Gains (**left**) and phase solutions (**right**) per antenna from bandpass calibration using the primary calibrator 's one scan.

## 2.3 Imaging

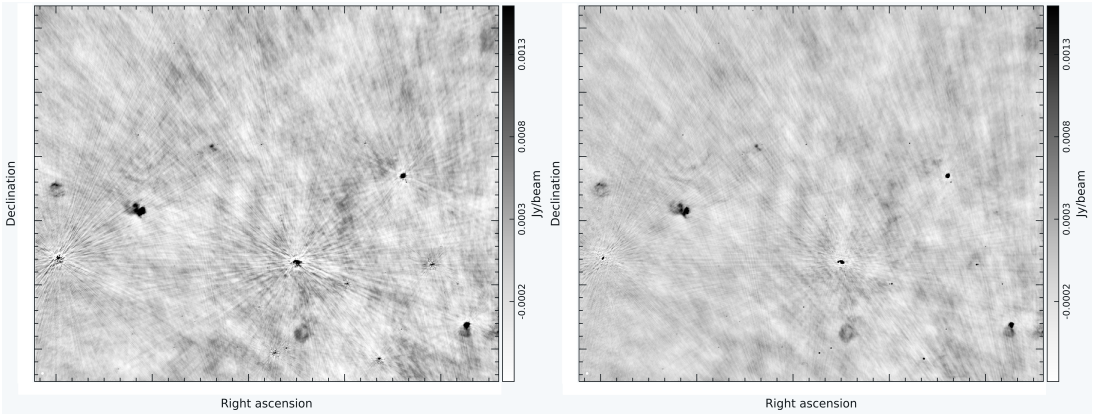


Figure 9: The reference calibrated image of the X-ray binary field (**left**) and the self-calibrated image (**right**). Both images are fixed at the same color-scale for comparison.

The calibrated, flagged data of the target field were imaged using *DDFacet* (Tasse et al., 2018) while self-calibration was performed with *killMS* (Smirnov & Tasse, 2015), a companion software of *DDFacet*. The image size was set at 15000 × 15000 pixels with each pixel spanning 0.15 arcsec in both X and Y directions. Briggs weighting was set with a robust parameter =

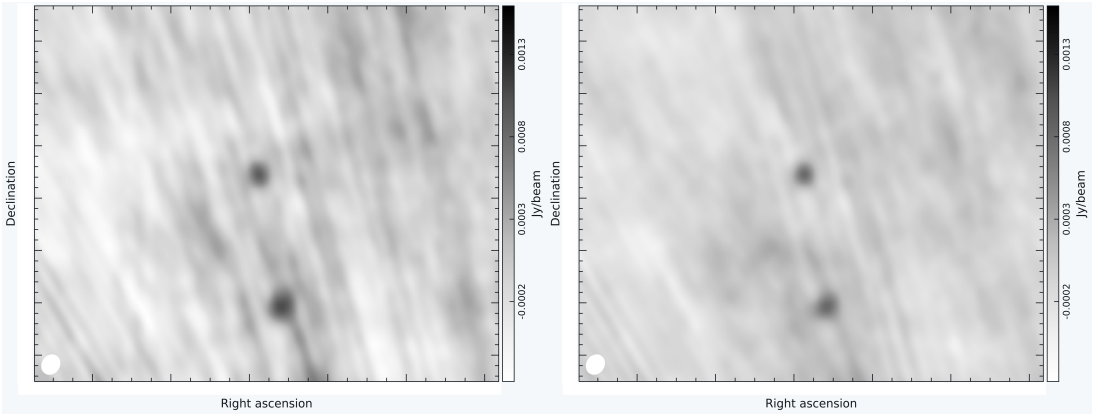


Figure 10: Zoom in at the phace center in the reference calibrated image of (**left**) and the self-calibrated image (**right**) where both north and south lobes are detected. Both images are fixed at the same color-scale for comparison. The beam size is 3.7 × 3.2 arcsec and it can be seen on the left corner of the images in white. Both images are fixed at the same color-scale for comparison.

-0.2. To improve the image quality, we phase self-calibrated with *killMS* and we re-imaged with *DDFacet* applying the *killMS* solutions. Figure 9 shows the reference calibrated image of the field at the left panel[7]. At the right panel, we see the improved by a factor of $\sim$ 20 % self-calibrated image. The angular resolution is 3.7 arcsec and the final rms noise of this complex field at 70$\mu$Jy level. Figure 10 illustrates a zoom in radio map at the centre of the target field showing the detection of our target. Both radio lobes were detected at 0.8mJy flux density.

As part of the ThunderKAT weekly observing run, the same field was observed on November 18, 2022 at L-band, two days before the current S-band observations. Figure 11 shows the comparison of the S-band with the L-band radio map of the target field highlighting the complexity of the field at low frequency (L-band). Similarly, we zoom in on the two radio lobes at the centre of the field in the Figure 12 showing the steep spectral index of the two radio jets that were detected at 2.7 mJy flux density at L-band. The resolution of the L-band radio map is 6.2 arcsec.

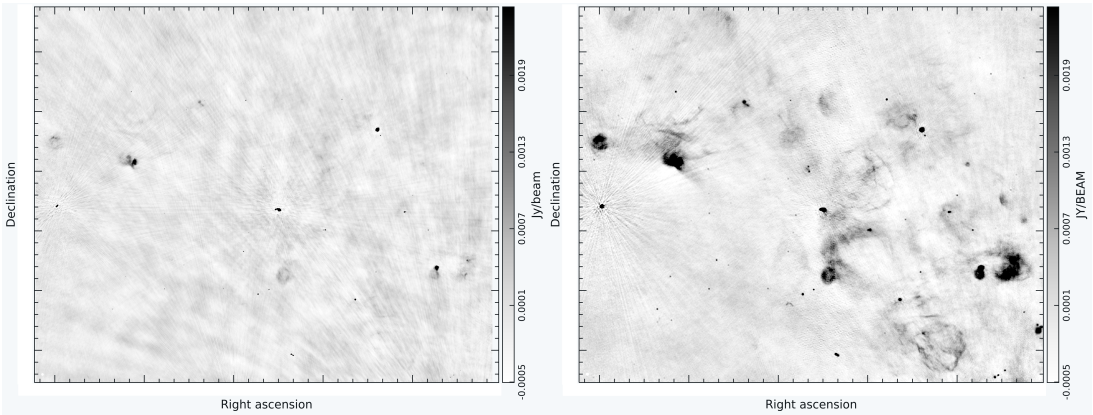


Figure 11: S-band radio map of the field using the data discussed here (**left**) and the L-band observations of the same field taken two days before as part of the regular weekend ThunderKAT observing run (**right**). Both images are fixed at the same color-scale for comparison.

## 3 Summary

We discussed here the recent MeerKAT S-band observations taken at the field of the X-ray binary, that is monitored regularly at L-band as part of the ThunderKAT observing run.

[7]The radio maps are visualized using the CARTA (Comrie et al., 2021) software (`https://cartavis.org/`)

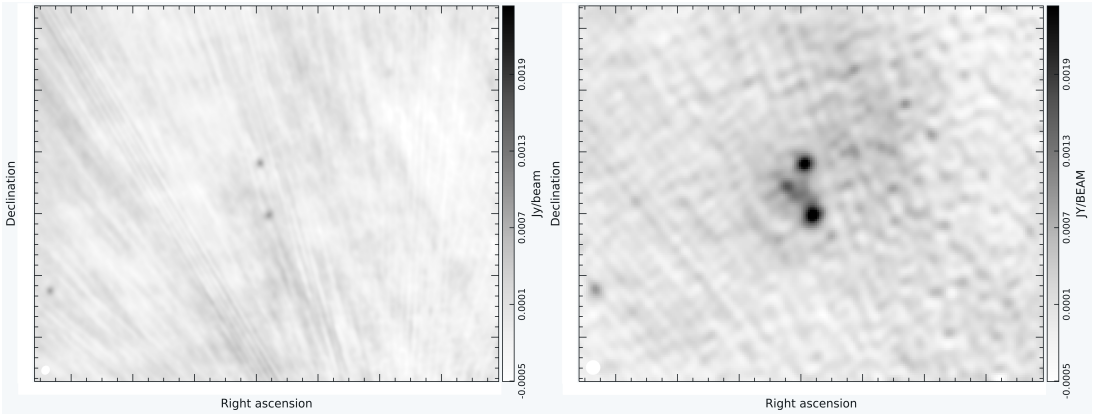


Figure 12: Zoom-in S-band radio map of the target field using the data discussed here (**left**) and similarly the L-band observations of the same field taken two days before as part of the regular weekend ThunderKAT observing run (**right**). Both images are fixed at the same color-scale for comparison.

The current observations used the S3 sub-band of the receiver, centred at 2843.8 MHz. The S3 sub-band does not seem to be dominated by RFI. The only interference seems to result from a continuous down-link signal from the GlobalStar satellite at around 2.5 GHz. However, it affects only the short baselines while the long baselines seem to be RFI clean and hence only 10% of the data were flagged in total.

The bandpass solutions remained pretty stable over the course of the observations and the secondary calibrator seems to be a good choice for future observations. The target field is a complex field with a lot of diffuse emission structures. The artefacts in the radio map resulted from the reference calibration were significantly improved by phase self-calibration.

Overall, the imaging capabilities at this high frequency with MeerKAT are impressive and although the targeted field is complex, the low RFI levels at this part of the band help to reach high sensitivity at $\sim 3$ arcsec angular resolution.

## References

Comrie A., et al., 2021, CARTA: The Cube Analysis and Rendering Tool for Astronomy, doi:10.5281/zenodo.4905459, https://doi.org/10.5281/zenodo.4905459

Fender R., et al., 2016, in MeerKAT Science: On the Pathway to the SKA. p. 13 (arXiv:1711.04132)

Matsuoka M., Kawai N., Imai T., Yamauchi M., Yoshida A., Kohno T., Yoneda A., Tsunemi H., 1990, in Kondo Y., ed., Astrophysics and Space Science Library Vol. 166, IAU Colloq. 123: Observatories in Earth Orbit and Beyond. p. 463, doi:10.1007/978-94-011-3454-5_65

McMullin J. P., Waters B., Schiebel D., Young W., Golap K., 2007, in Shaw R. A., Hill F., Bell D. J., eds, Astronomical Society of the Pacific Conference Series Vol. 376, Astronomical Data Analysis Software and Systems XVI. p. 127

Offringa A. R., van de Gronde J. J., Roerdink J. B. T. M., 2012, A&A, 539

Smirnov O. M., Tasse C., 2015, MNRAS, 449, 2668

Tasse C., et al., 2018, A&A, 611, A87